Effect of annealing treatment on properties of Ce-doped indium oxide (ICO) transparent conductive oxide films

Huan Liu[1,2] , Yuanbo Gong[4], Hongwei Diao[2], Xiaojie Jia[2], Lei Zhao[2,3,5,*], Wenjing Wang[2,3,5], Wei Wang[4], and Jun Zong[4]

[1] *Yangtze Delta Region Institute (Huzhou), University of Electronic Science and Technology of China, Huzhou 313001, China*
[2] *Key Laboratory of Solar Thermal Energy and Photovoltaic System of Chinese Academy of Sciences, Institute of Electrical Engineering, Chinese Academy of Sciences, Beijing 100190, China*
[3] *University of Chinese Academy of Sciences, Beijing 100049, China*
[4] *Spic New Energy Science and Technology Co., Ltd, Nanchang 330096, China*
[5] *Dalian National Laboratory for Clean Energy, the Chinese Academy of Sciences, Dalian 116023, China*

ABSTRACT

Ce-doped indium oxide films were prepared by reactive plasma deposition, and the effects of annealing temperature and annealing time on the electrical properties, optical properties, and film structure of the ICO films were investigated. The study found that the annealing treatment was beneficial to improve the crystallinity, the grain size, the transmittance of the films, and to reduce the resistivity of the films. When the ICO films were annealed at 210 °C in air for 50 min, the mobility of 93.3 $cm^2/V s$, a carrier concentration of $2.48 \times 10^{20}/cm^3$, an average transmittance of 86.5%, and the resistivity of 2.6×10^{-4} Ω cm were obtained. The ICO films presented higher carrier mobility and lower carrier concentration than the Sn-doped In_2O_3 (ITO) films, which are conducive to improving the efficiency of solar cells.

1 Introduction

Recently, Ce-doped In_2O_3 (ICO) transparent conductive oxide (TCO) films [1–3] have attracted more and more attention because of their higher carrier mobility (μ_e), lower resistivity (ρ), and higher optical transmittance [4–8]. In 2014, Kang et al. [9] used magnetron sputtering to prepare Sn-doped In_2O_3 (ITO) film and ICO film. They studied the influence of film thickness and Ce concentration on film properties. Since the Ce–O bond enthalpy (795 ± 8 kJ/mol) is higher than the In–O bond enthalpy (320.1 ± 41.8 kJ/mol) and the Sn–O bond enthalpy (531.8 ± 12.6 kJ/mol), the ICO film is easier to nucleate than the ITO film during the deposition process. Ce doping changes the growth mode of the film [9]. By optimizing the parameters, the best μ_e of the ICO film is ~ 50 $cm^2/V s$. In 2016, An et al. [10] studied the influence of substrate temperature and found that the optical and electrical properties of ICO were better than ITO films. As the substrate temperature increases, the ICO film changes from

amorphous to polycrystalline. When the substrate temperature is 150 °C, the highest mobility of ICO film is 84.3 cm^2/V s. They applied ICO film instead of ITO film onto perovskite and silicon tandem cells, and the cell efficiency increased from 18.85% to 20.37%. In 2018, Shi et al. [11] used reactive plasma deposition (RPD) to prepare ICO films. They studied the influence of ICO film thicknesses on carrier concentration (N_e) and μ_e. It is found that as the film thickness increases, the N_e increases, and the μ_e first increases and then decreases. When the film thickness is 30 nm, the maximum μ_e is 153.7cm^2/V s, and the N_e is 1.9×10^{20}/cm^3. They believe that when the film thickness is less than 30 nm, the μ_e is affected by the surface scattering mechanism, and when the film thickness is thicker than 50 nm, the μ_e is affected by the grain boundary scattering mechanism. In 2019, Mei et al. [12] used magnetron sputtering to prepare ICO films and studied the effects of Ce doping with different concentrations on the optical and electrical properties of TCO films. They found that Ce doping can change the nucleation and growth processes of TCO film. The grain growth of ICO film is oriented along the [111], and as the deposition time increases, the film tends to grow along the [100]. In addition, Ce doping can weaken crystallinity, reduce surface roughness, and increase the density of TCO film. Surface scattering is dominant in amorphous ICO, and ionized impurity scattering is dominant in polycrystalline ICO. ICO film shows excellent performance, which is worth studying.

In fact, most TCO films are prepared by physical vapor deposition (PVD) [13–15]. However, TCO films prepared by RPD with denser structures, higher crystallinity, smoother surface, higher conductivity, and better optical transmittance [16, 17]. In this paper, ICO films were prepared by RPD, and the effects of annealing temperature and annealing time on the electrical properties, optical properties, and film structure of ICO films were studied. By optimizing the experimental parameters, the film with the best performance was obtained, and the mechanism of annealing temperature and annealing time was explored.

2 Experimental

ICO films with a thickness of about 100 nm were prepared on glass substrates by RPD (Archers RPD-1Gun) with the targets composed of 97.0% In$_2$O$_3$: 3.0% CeO$_2$ in weight. The film deposition conditions were as follows: O$_2$ concentration (the percentage of O$_2$ in the total amount of O$_2$ and Ar) 18.5%, the current density of the plasma gun 160 A/m^2, and the deposition pressure 1.5 mTorr. The samples were prepared at room temperature and then annealed in air. When studying the effect of annealing temperature, the fixed annealing time was 50 min, and the annealing temperature was 170–250 °C. When the effect of annealing time was studied, the fixed annealing temperature was 210 °C, and the annealing time was 10–90 min.

The optical transmittance of ICO films was measured in the wavelength range of 300–1200 nm via ultraviolet–visible spectrophotometer (UV-2600), the thickness was obtained via ellipsometer (Raditech SE-950), the ρ, the N_e and the μ_e were acquired via Hall measurement (Swin HALL8800-II). Further, the film crystallinity was analyzed via X-ray diffractometer (XRD D8 ADVANCE).

3 Results and discussion

3.1 The effect of annealing temperature on the properties of ICO films

Figure 1 shows the effect of annealing temperature on the electrical properties of ICO films. We found that the as-deposited films had a high ρ of $\sim 4.6 \times 10^{-4}$ Ω cm, but the ρ decreased significantly after annealing with the ρ of $\sim 2.5 \times 10^{-4}$ Ω cm. It is consistent with the results reported in the literature [18]. However, in our previous study [19], the lowest ρ of ITO is $\sim 9.6 \times 10^{-4}$ Ω cm, which shows that ICO has better electrical performance. With the increase of annealing temperature, the ρ decreased more obviously. The change in ρ is determined by the N_e and μ_e. ρ is calculated according to the following Eq. (1).

$$\rho = \frac{1}{q\mu_e N_e} \quad (1)$$

where, q is the quantity of electric charge ($q = 1.6 \times 10^{-19}$C). When the annealing temperature
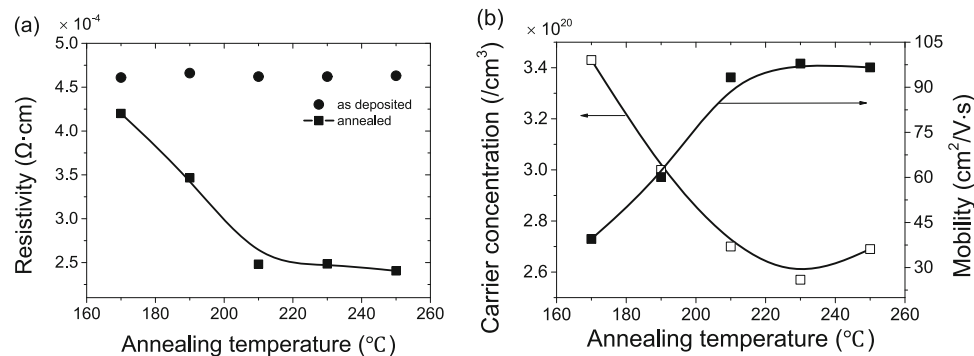
Fig. 1 a The resistivity (ρ) of ICO films obtained before and after annealing as functions of the annealing temperature, the circle represents the ρ of the as-deposited film, and the square represents the ρ of the film after annealing, **b** the carrier concentration (N_e) and the carrier mobility (μ_e) of the annealed ICO films as functions of the annealing temperature

is lower, the μ_e is lower, which results in higher ρ. As the annealing temperature increases, the increase in μ_e is larger than the decrease in N_e, resulting in a decrease in ρ. The N_e is related to the concentration of oxygen vacancies [16, 20, 21] and activated Ce^{4+} [22]. Studies have shown that [23] there is a dynamic process of adsorption and desorption of oxygen atoms in the film when annealed in air. When the number of oxygen atoms adsorbed in the film is more than the number of oxygen atoms removed, the oxygen vacancies in the film decrease, resulting in a decrease in the N_e. Conversely, the N_e increases. As the annealing temperature increases, the number of oxygen atoms in the air entering the film increases, resulting in a decrease in the N_e. However, with the increase of annealing temperature, the number of activated Ce^{4+} increased, increasing in the N_e. In general, the N_e increases slightly at higher temperatures because of the increase of activated Ce^{4+}. At the same time, we found that as the annealing temperature increased, the μ_e increased and then remained unchanged. When the annealing temperature is higher than 210 °C, the μ_e reaches about 95 cm^2/V s.

Figure 2 shows the effect of annealing temperature on the optical properties of ICO films. The average transmittance of the film was calculated from the transmittance spectrum in the wavelength range of 400–1100 nm. It can be seen that when the annealing temperature is higher than 190 °C, the average transmittance of the film increases with the increase of the annealing temperature, and the average transmittance is higher than 85%. And from the transmittance spectrum, the transmittance in the full spectrum range increases with the increase of the annealing temperature. The transmittance is affected

by the thickness and N_e. From the above results, the N_e decreases with the increase of annealing temperature, so less free-carrier absorption leads to an increase in the transmittance. However, a slight increase in thickness leads to a decrease in transmittance at 190 °C.

In order to explore the effect of annealing temperature on the structure of ICO films, we analyzed the film crystallinity via XRD. Figure 3a shows that the diffraction peaks of each sample at different annealing temperatures are consistent with the standard XRD spectrum of In_2O_3 (JCPDS No. 06-0416). It shows that no new compound is formed, and the film is polycrystalline. As the annealing temperature increases, the diffraction peak intensity of the (222) plane increases, indicating that the crystallinity of the film is improved. It can be seen from Fig. 3b that as the annealing temperature increases, the center position of the diffraction peak of the (222) crystal plane moves to a large angle, and when the annealing temperature is 250 °C, it moves to a small angle. The change of the center position of the diffraction peak mainly reflects the change of the stress in the film [24, 25]. Properly increasing the annealing temperature is beneficial to reduce the internal stress of the film, but when the annealing temperature is too high, the film stress increases. Figure 3c shows the grain size (D) and the full width at half maximum (FWHM). The D corresponding to the (222) diffraction peak was quantitatively characterized according to the Scherrer formula [19].

$$D = \frac{K\gamma}{B\cos\theta} \tag{2}$$

where, K is the Scherrer constant ($K = 0.89$), B is the FWHM of the diffraction peak, θ is the diffraction

Fig. 2 **a** The average transmittance of the annealed ICO films as a function of different annealing temperatures, **b** the transmittance spectrum of the annealed ICO films as a function of wavelength for different annealing temperatures
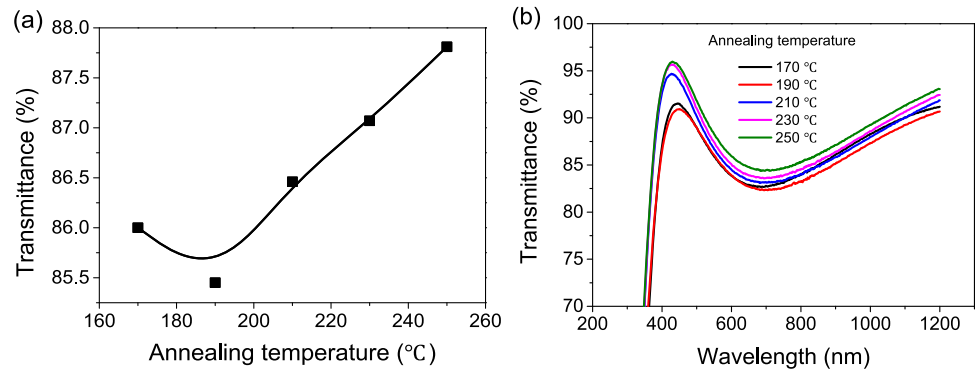
Fig. 3 **a** XRD curves of the annealed ICO films obtained with different annealing temperatures, **b** XRD curves of (222) crystal plane, **c** the corresponding grain size (D) and the full width at half maximum (FWHM) calculated for the ICO films
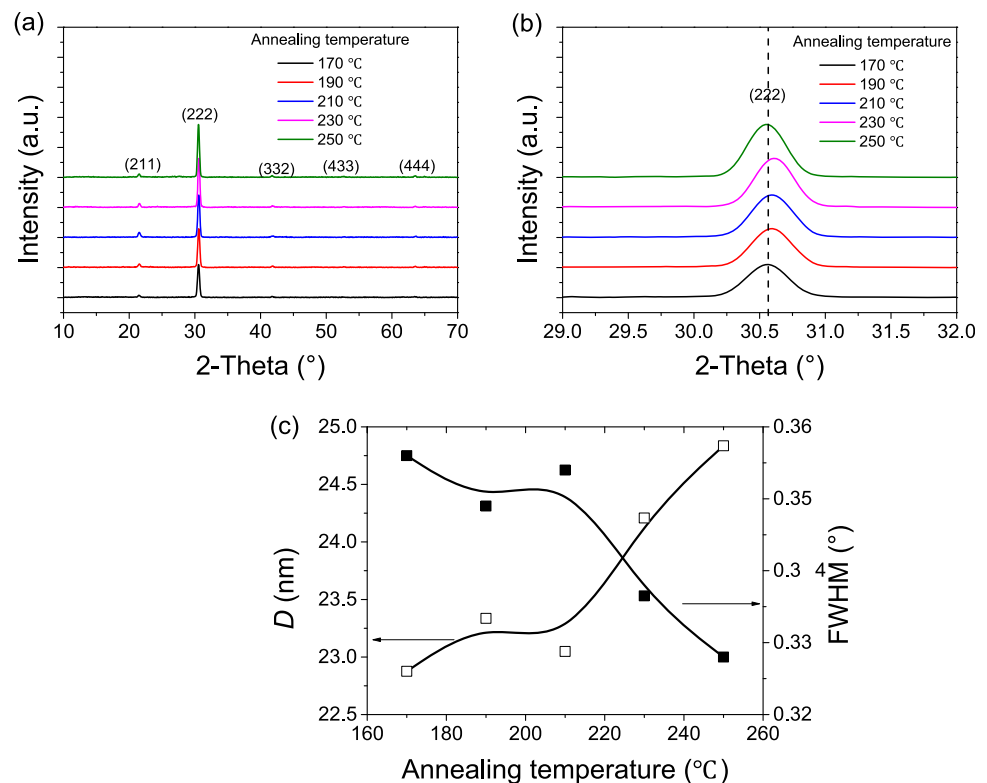
angle, and γ is the X-ray wavelength ($\gamma = 1.54$ Å). As the annealing temperature increases, the D increases and the FWHM decreases, which indicates that the crystallinity of the film is improved. The μ_e mainly depends on lattice vibration, neutral impurity scattering, ionized impurity scattering, and grain boundary scattering [26, 27]. The increase of D is beneficial to reduce the grain boundary scattering and improve the μ_e. This result is also consistent with the Hall result above.

Considering the influence of annealing temperature on the electrical properties, optical properties, film structure, and fabrication cost of ICO films. The optimal annealing temperature is 210 °C, and the

obtained ICO film was with the μ_e of 93.3 cm^2/V s, the N_e of 2.48×10^{20}/cm^3, the average transmittance of 86.5%, and the ρ of 2.6×10^{-4} Ω cm, which is better than the ITO film with the μ_e of 24.1 cm^2/V s, the N_e of 2.7×10^{20}/cm^3, the average transmittance of 86.0%, and the ρ of 9.6×10^{-4} Ω cm [19].

3.2 The effect of annealing time on the properties of ICO films

Figure 4 shows the effect of annealing time on the electrical properties of ICO films. As the annealing time increases, the ρ decreases continuously. When the annealing time is shorter, lower N_e and μ_e lead to

higher ρ. As the annealing time increases, the number of desorbed oxygen atoms in the film is larger than the number of adsorbed oxygen atoms, which increases the oxygen vacancy concentration and the N_e. The energy accumulation in the film causes the concentration of activated Ce^{4+} to rise as annealing time rises, which leads to an increase in N_e. The μ_e increases and then decreases with increasing annealing time. The main reason is that the increase of the activated Ce^{4+} leads to the enhanced scattering of ionized impurities and the decrease of the μ_e. In addition to this, annealing for too long may cause lattice vibrations or introduce new defects [28], which reduce μ_e.

Figure 5 shows the relationship between annealing time and ICO films' transmittance. When the annealing time is longer than 30 min, the average transmittance of the film increases with the increase of the annealing time. Meanwhile, from the transmittance spectrum, the transmittance of the long wavelength increases with the increase of annealing time. The transmittance of the thin film is related to the absorption and reflection of the film. With the change of film crystallinity, grain size, etc., the transmittance of the film changes.

We also analyzed the film crystallinity via XRD, as shown in Fig. 6a, there is no new material generated after annealing and the film is polycrystalline. The diffraction peak intensity of the (222) plane increases with the annealing time increases, indicating that the crystallinity of the film is improved. It can be seen from Fig. 6b that as the annealing time increases, the center position of the diffraction peak of the (222) crystal plane moves to a large angle, which indicates

that the internal stress of the film is released. Figure 6c shows the relationship between the D or the FWHM and the annealing time. As the annealing time increases, the D increases, resulting in decreased grain boundary scattering and increased μ_e. With the increase of annealing time, the FWHM decreases, which also indicates that the crystallinity of the film is improved.

From the perspective of high μ_e and low N_e, ICO films with better performance can be obtained with an annealing time of 50 min. Under these conditions, the μ_e of the ICO film was 93.3 cm^2/V s, the N_e was 2.48×10^{20}/cm^3, the average transmittance was 86.5%, and the ρ was 2.6×10^{-4} Ω cm.

4 Conclusion

It was found that the annealing temperature and annealing time significantly affected the electrical properties, optical properties, and film structure of ICO films. During the annealing process, there is recombination, recrystallization, and film stress relief. As the annealing temperature increases, the crystallinity of the film improves and the D increases, resulting in decreased grain boundary scattering, increased μ_e, and decreased ρ. At the same time, as the temperature increase, the N_e decreases, which improves the transmittance of the film. However, when the annealing temperature is too high, other defects may be caused. As the annealing time increases, the film stress is released, the crystallinity improves, and the D increases, resulting in decreased grain boundary scattering and increased μ_e. However, when the annealing time is too long, more
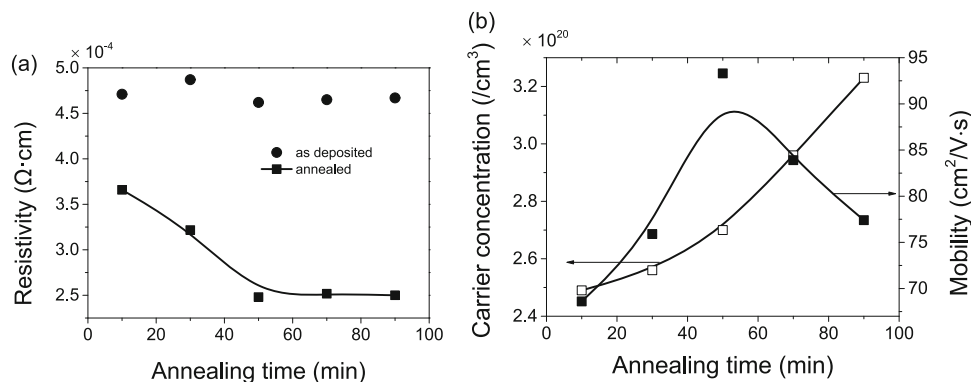

Fig. 4 a The resistivity (ρ) of ICO films obtained before and after annealing as functions of the annealing time, the circle represents the ρ of the as-deposited film, and the square represents the ρ of

the film after annealing, **b** the carrier concentration (N_e) and the carrier mobility (μ_e) of the annealed ICO films as functions of the annealing time

Fig. 5 a The average transmittance of the annealed ICO films as a function of different annealing times, **b** the transmittance spectrum of the annealed ICO films as a function of wavelength for different annealing times
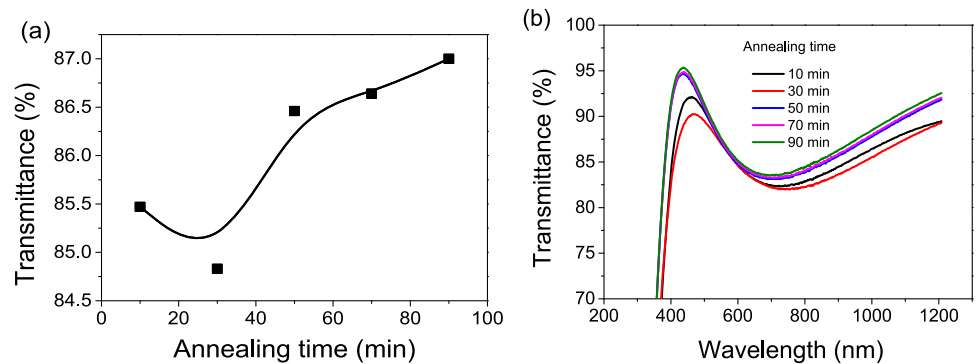
Fig. 6 a XRD curves of the annealed ICO films obtained with different annealing times, **b** XRD curves of (222) crystal plane, **c** the corresponding grain size (D) and full width at half maxima (FWHM) calculated for the ICO films
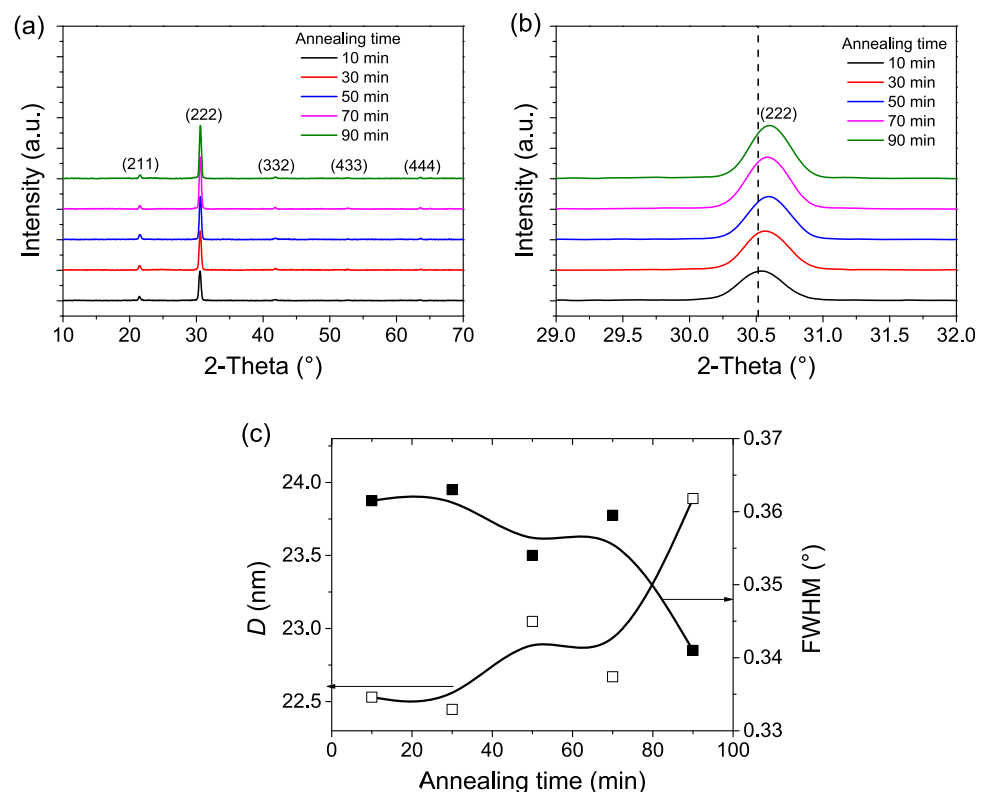
oxygen atoms are desorbed or more activated Ce^{4+} in the film, resulting in a higher N_e. There are potential barriers at the grain boundaries that trap free carriers and reduce μ_e. By optimizing the annealing process, we obtain the best performance ICO films after annealing at 210 °C in air for 50 min. The μ_e of the ICO film was 93.3 $cm^2/V\,s$, the N_e was $2.48 \times 10^{20}/cm^3$, the average transmittance was 86.5%, and the ρ was $2.6 \times 10^{-4}\ \Omega\ cm$. ICO films have better performance than traditional ITO films for solar cells.

Author contributions

Conceptualization: LZ; methodology: YG, LZ, WW; formal analysis and investigation: YG, HL; writing—original draft preparation: HL; writing—review and editing: HL, XJ, HD, LZ, WW; funding acquisition: LZ, WW, JZ; resources: WW, JZ; supervision: WW, JZ.

Funding

Data availability

All data generated or analysed during this study are included in this published article.

Declarations

Conflict of interest The authors have no relevant financial or non-financial interests to disclose.

References

1. J. Sun et al., J. Mater. Sci. **32**, 27290–27304 (2021). https://doi.org/10.1007/s10854-021-07099-4
2. X. Liu et al., Appl. Surf. Sci. **428**, 478–484 (2018). https://doi.org/10.1016/j.apsusc.2017.09.177
3. X. Chen et al., J. Nanopart. Res. (2019). https://doi.org/10.1007/s11051-019-4516-3
4. L. Tutsch et al., Prog Photovolt. **29**, 835–845 (2021). https://doi.org/10.1002/pip.3388
5. K. Dey et al., Ceram. Int. **47**, 1798–1806 (2021). https://doi.org/10.1016/j.ceramint.2020.09.006
6. Y. Watabe, E. Kobayashi. 29th European Photovoltaic Solar Energy Conference and Exhibition (2014). https://doi.org/10.4229/eupvsec20142014-2bo.4.2.
7. E. Kobayashi et al., Sol. Energy Mater. Sol. Cells. **149**, 75–80 (2016). https://doi.org/10.1016/j.solmat.2016.01.005
8. B.H. Kim et al., ACS Nano **12**, 3200–3208 (2018). https://doi.org/10.1021/acsnano.7b06783
9. S. Kang, S. Cho, P. Song, Thin Solid Films **559**, 92–95 (2014). https://doi.org/10.1016/j.tsf.2013.11.056
10. S. An et al., Sol. Energy **196**, 409–418 (2020). https://doi.org/10.1016/j.solener.2019.12.040
11. J. Shi et al., Mater. Lett. **225**, 54–56 (2018). https://doi.org/10.1016/j.matlet.2018.04.102
12. Mei, F. et al. Appl. Surf. Sci. **509**, 144810 (2020). https://doi.org/10.1016/j.apsusc.2019.144810.
13. H. Wang et al., Appl. Surf. Sci. **503**, 144273 (2020). https://doi.org/10.1016/j.apsusc.2019.144273
14. A.V. Vasin et al., Vacuum **174**, 109199 (2020). https://doi.org/10.1016/j.vacuum.2020.109199
15. R.S. Santiago et al., Thin Solid Films. **700**, 137917. https://doi.org/10.1016/j.tsf.2020.137917 (2020).
16. K.Y. Chen, S.P. Chang, C.H. Lin, RSC Adv. **9**, 87–90 (2019). https://doi.org/10.1039/c8ra08803a
17. J. Yu et al., Sol. Energy Mater. Sol. Cells. **144**, 359–363 (2016). https://doi.org/10.1016/j.solmat.2015.09.033
18. N.M. Ahmed et al., Results. Phys. **13**, 102159 (2019). https://doi.org/10.1016/j.rinp.2019.102159
19. H. Liu et al., J. Mater. Sci. **33**, 5000–5008 (2022). https://doi.org/10.1007/s10854-021-07689-2
20. W. Huang et al., J. Alloys Compd. **843**, 155151 (2020). https://doi.org/10.1016/j.jallcom.2020.155151
21. J. Yu et al., Jpn. J. Appl. Phys. (2017). https://doi.org/10.7567/jjap.56.08mb09
22. J. Shi, Shanghai Institute of Microsystem and Information Technology, Chinese Academy of Sciences (2018).
23. L. Shen, Shanghai Institute of Microsystem and Information Technology, Chinese Academy of Sciences (2016).
24. K. Ellmer et al., Solid State Phenom. **51–52**, 541–546 (1996). https://doi.org/10.4028/www.scientific.net/SSP.51-52.541
25. M.K. Puchert et al., J. Vac. Sci. Technol. A. **14**, 2220–2230 (1996). https://doi.org/10.1116/1.580050
26. Z.L. Pei et al., J. Appl. Phys. **90**, 3432–3436 (2001). https://doi.org/10.1063/1.1398070
27. E. Shanthi et al., J. Appl. Phys. **51**, 6243–6251 (1980). https://doi.org/10.1063/1.327610
28. J.H. Mackey, H.L. Smith, A. Halperin, J. Phys. Chem. Solids. **27**, 1759–1772 (1966). https://doi.org/10.1016/0022-3697(66)90107-7